Low-loss broadband bi-layer edge couplers for visible light

YIDING LIN,[1,*] JASON C. C. MAK,[2] HONG CHEN,[1] XIN MU,[1,2]
ANDREI STALMASHONAK,[1] YOUNGHO JUNG,[1] XIANSHU LUO,[3]
PATRICK G.-Q. LO,[3] WESLEY D. SACHER,[1] AND JOYCE K. S.
POON[1,2]

[1]*Max Planck Institute of Microstructure Physics, Halle (Saale) 06120, Germany*
[2]*Department of Electrical and Computer Engineering, University of Toronto, 10 King's College Road, Toronto, Ontario M5S 3G4, Canada*
[3]*Advanced Micro Foundry Pte Ltd, 11 Science Park Road, Singapore Science Park II, 117685, Singapore*
*yidinlin@mpi-halle.mpg.de

Abstract: Low-loss broadband fiber-to-chip coupling is currently challenging for visible-light photonic-integrated circuits (PICs) that need both high confinement waveguides for high-density integration and a minimum feature size above foundry lithographical limit. Here, we demonstrate bi-layer silicon nitride (SiN) edge couplers that have ≤ 4 dB/facet coupling loss with the Nufern S405-XP fiber over a broad optical wavelength range from 445 to 640 nm. The design uses a thin layer of SiN to expand the mode at the facet and adiabatically transfers the input light into a high-confinement single-mode waveguide (150-nm thick) for routing, while keeping the minimum nominal lithographic feature size at 150 nm. The achieved fiber-to-chip coupling loss is about 3 to 5 dB lower than that of single-layer designs with the same waveguide confinement and minimum feature size limitation.

1. Introduction

Photonic-integrated circuits (PICs) operating in the visible light spectrum hold great promise in a growing number of applications beyond telecommunications, including integrated neurophotonics for optogenetics and brain imaging [1–5], integrated ion traps for quantum information processing [6,7], and potential miniaturized display systems for augmented and virtual reality [8–10]. Efficient light coupling from a launching fiber to the PIC is critical to expand optical power budgets into the PIC, which enriches design potential for these applications. Currently, two types of fiber-to-chip couplers, namely, edge couplers [11–13] and surface grating couplers [14–16] are commonly adopted in state-of-the-art PICs. Each type of couplers has its advantages [17,18]. For example, compared to grating couplers, edge couplers typically have a higher coupling efficiency, broader optical bandwidth, and lower polarization dependent loss. Grating couplers are more convenient for on-wafer testing, can be placed anywhere on-chip, and often have a higher tolerance to fiber misalignment. For the visible spectrum, edge couplers are usually preferred over grating couplers in applications where a large optical bandwidth covering a broad wavelength range (~400–700 nm) or in-plane packaging (such as in photonic neuroprobes [2] and quantum ion traps [6]) are needed.

A challenge to efficient fiber-to-chip edge coupling is the mode mismatch between the on-chip waveguide and the fiber. For example, at a blue wavelength (λ) of 488 nm, the mode is tightly confined in a ~200×280 nm silicon nitride (SiN) waveguide [19]. The small mode field diameter (MFD) leads to a significant mode mismatch loss when coupling the light from, for example, a Nufern S405-XP single-mode fiber with a $1/e^2$ MFD of ~3.7 µm ($\lambda = 488$ nm). To match the MFD with that of the fiber, one may adopt an inverse tapered design for the coupler [20], but
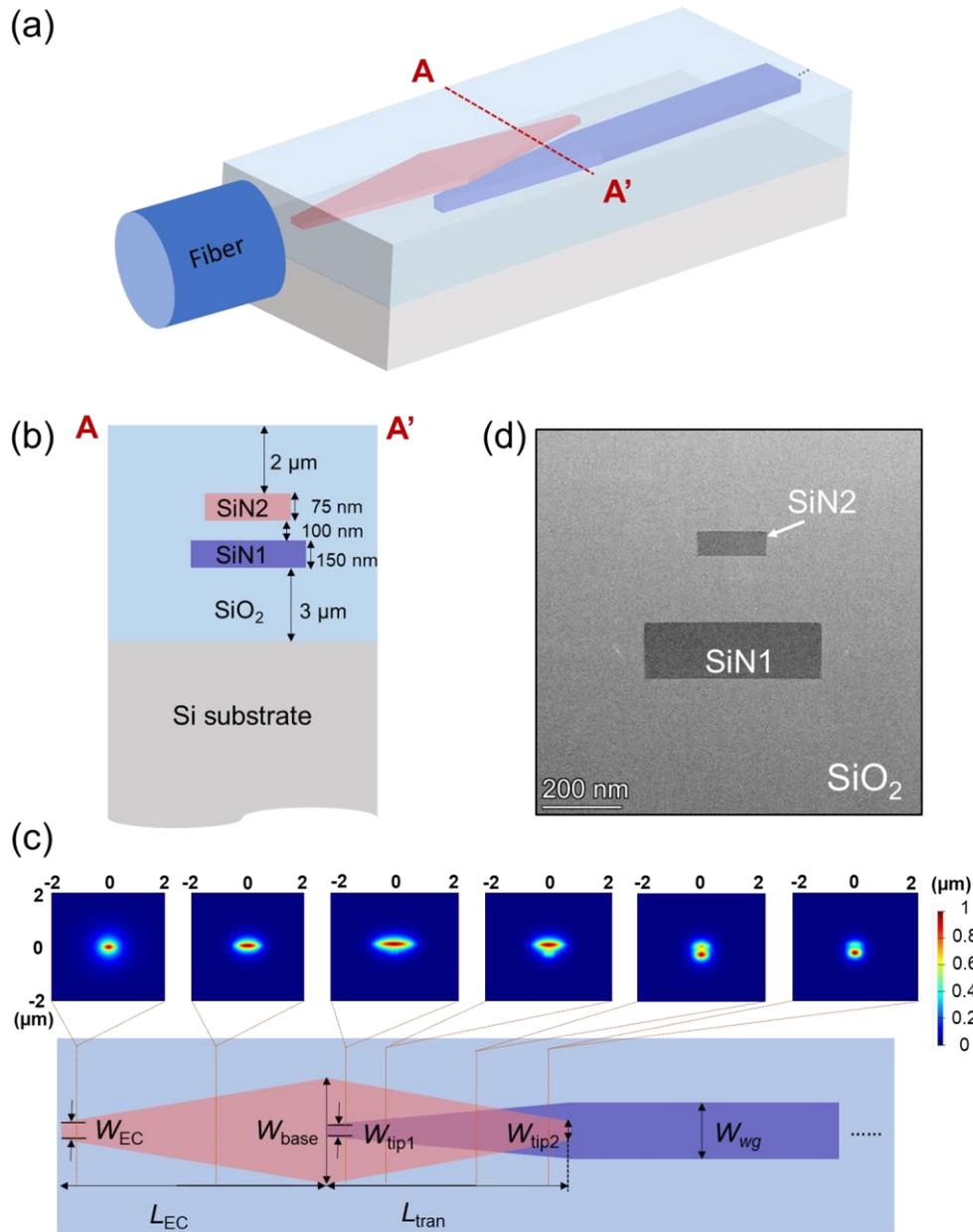
Fig. 1. (a) Three-dimensional (3-D) schematic of a bi-layer SiN edge coupler. A cross-sectional schematic of the coupler along AA' is shown in (b). (c) Top-view schematic of the bi-layer coupler. Corresponding design parameters are labelled for the discussion and optimization in subsequent sections. The mode profiles at top depict the fundamental TE mode evolution in an optimized bi-layer coupler as the light propagates through ($\lambda = 488$ nm). (d) A cross-sectional TEM image of a fabricated bi-layer edge coupler along AA'.

presently, the tip width of such an inverse taper (~75 nm) is too narrow to be reliably fabricated in current silicon photonic foundries [21]. Recent reports [22–24] have utilized a thin (~20 nm) SiN to maintain both a large MFD and a feature size above the deep ultraviolet (DUV) lithographic

limit. However, the reduced mode confinement leads to millimeter-scale bend radii, hindering high-density PIC integration.

In infrared silicon (Si) photonics, spot-size converters, incorporating lower-index (e.g., SiO_x [25], SiN [26,27], SiON [28,29] and polymers [30–33]) waveguides or tapers, are overlaid on Si waveguides [34] for the MFD expansion in edge couplers. However, to our knowledge, this concept has so far not been investigated for visible spectrum photonic platforms.

In this work, we overcome the trade-offs among fiber-to-chip mode mismatch, lithographical-limited feature size and on-chip mode confinement in visible-light edge couplers by adopting an auxiliary thin SiN [SiN2, 75 nm, in Fig. 1(b)] waveguide atop a thicker one (SiN1, 150 nm). The thin SiN2 layer supports an expanded MFD at a feature size compatible with foundry fabrication to enable efficient light coupling from the fiber. The coupled light is then transferred to the thick SiN1 layer via an interlayer adiabatic tapered transition, and the SiN1 serves as the main waveguide routing layer in a PIC. The fabricated bi-layer edge couplers show a coupling loss ≤ 4.0 dB/facet over a broad spectrum of $\lambda = 445$–640 nm, which is a ~3–5 dB improvement compared to that of single-layer (SiN1 only) tapered couplers. A SiN2-SiN1 interlayer transition loss was < 0.5 dB across the visible spectrum. This work paves the way towards visible-light PICs with an increased optical power budget and a higher integration density. The bi-layer structure can be extended to multi-layer designs comprising other waveguide materials (e.g. $LiNbO_3$ [35], AlN [36], TiO_2 [37], Al_2O_3 [38–40] and Ta_2O_5 [41] etc.) to further optimize the coupling efficiency.

2. Design and fabrication of the bi-layer SiN edge coupler

Figure 1(a) shows a three-dimensional (3-D) schematic of the bi-layer SiN edge coupler, where a cross-sectional schematic of the coupler along AA' is shown in Fig. 1(b). The SiN layers were defined with silicon dioxide (SiO_2) cladding on the Si substrate. The nominal interlayer spacing between SiN1 and SiN2 was 100 nm. The bottom and top cladding thicknesses were 3 and 2 μm, respectively, to the Si substrate and the superstrate (air). Figure 1(c) depicts a top-view schematic of the bi-layer edge coupler. The coupler starts in the 75-nm thick SiN2 layer with an inverse taper at a tip width W_{EC}, adiabatically widening to a base width W_{base} over a length L_{EC}. The light is then transferred to a single-mode 150-nm thick SiN1 routing waveguide with a width W_{wg} via an adiabatic SiN2-SiN1 interlayer transition (length: L_{tran}; tip width: $W_{tip1} = W_{tip2} = 0.15$ μm). The mode profiles in the inset of Fig. 1(c) illustrate the evolution of the fundamental TE mode in an optimized bi-layer coupler at $\lambda = 488$ nm ($W_{EC} = 0.20$ μm, $W_{base} = 0.75$ μm, $L_{EC} = 200$ μm, $L_{tran} = 75$ μm, $W_{wg} = 0.38$ μm). We used a bend radius of 80 μm for routing the SiN1 waveguides and found the bend loss to be negligible compared to the SiN1 propagation loss. On a separate wafer run with SiN1 waveguide thickness of 0.12 μm and W_{wg} of 0.40 μm, the loss for 20-μm radius bends was measured to be 0.05 ± 0.02 (TM) and 0.04 ± 0.01 (TE) dB per 90° bend at $\lambda = 488$ nm using the cutback method. A smaller bend radius with low loss supports high-density PIC integration.

The bi-layer couplers were fabricated on 200-mm diameter Si wafers at Advanced Micro Foundry. Both SiN1 and SiN2 (measured refractive index ~1.82 at $\lambda = 488$ nm), together with the SiO_2 cladding (measured refractive index ~1.46 at $\lambda = 488$ nm), were deposited via plasma enhanced chemical vapour deposition (PECVD). The SiN layers were patterned by DUV (ArF) lithography and reactive-ion etching. Chemical-mechanical polishing (CMP) was performed after each deposition step, except the top SiO_2 cladding layer, for planarization. Focused-ion beam milling was used to reveal the cross-section of the fabricated structure. Figure 1(e) shows a cross-sectional transmission electron microscope (TEM) image of the coupler along AA' [in Fig. 1(a)]. The fabricated layer thicknesses agree well with the nominal designed values.

In the following subsections, we discuss the optimization of several key design parameters determining the coupling efficiency of bi-layer SiN edge couplers. Unless otherwise stated, for the calculations, a design wavelength of 488 nm and $W_{wg} = 0.38$ μm are nominally assumed.

2.1. Effect of SiN2 tip width (W_{EC})

The SiN2 tip width (W_{EC}) determines the mode overlap between the edge coupler and the launching fiber mode. Here we calculated the fiber-to-tip power coupling efficiency (η_{pc}) using the mode overlap calculation in a finite difference eigenmode (FDE) solver with the nominal SiN2 thickness (75 nm) and measured material refractive indices. A Gaussian beam profile was assumed for the fiber (Nufern S405-XP, identical to that used in subsequent characterizations) with an estimated MFD of 3.72 µm at $\lambda = 488$ nm (see Supplement 1, Section S1). A corresponding beam profile is shown in Fig. 2(a). Figure 2(b) shows the calculated fundamental TE and TM mode profiles in SiN2 with respect to W_{EC}. The MFD increases with decreasing W_{EC}, which explains the η_{pc} enhancement in Fig. 2(c) with W_{EC} decreased from 0.35 to 0.15 µm. The η_{pc} drops with the further decrease of W_{EC}, as the MFD of the SiN2 tip becomes larger than that of the fiber. Hence, an optimal fiber-to-tip coupling (TM$_0$: ~92%, TE$_0$: ~87%) can be found at a W_{EC} of 0.15 µm at $\lambda = 488$ nm.
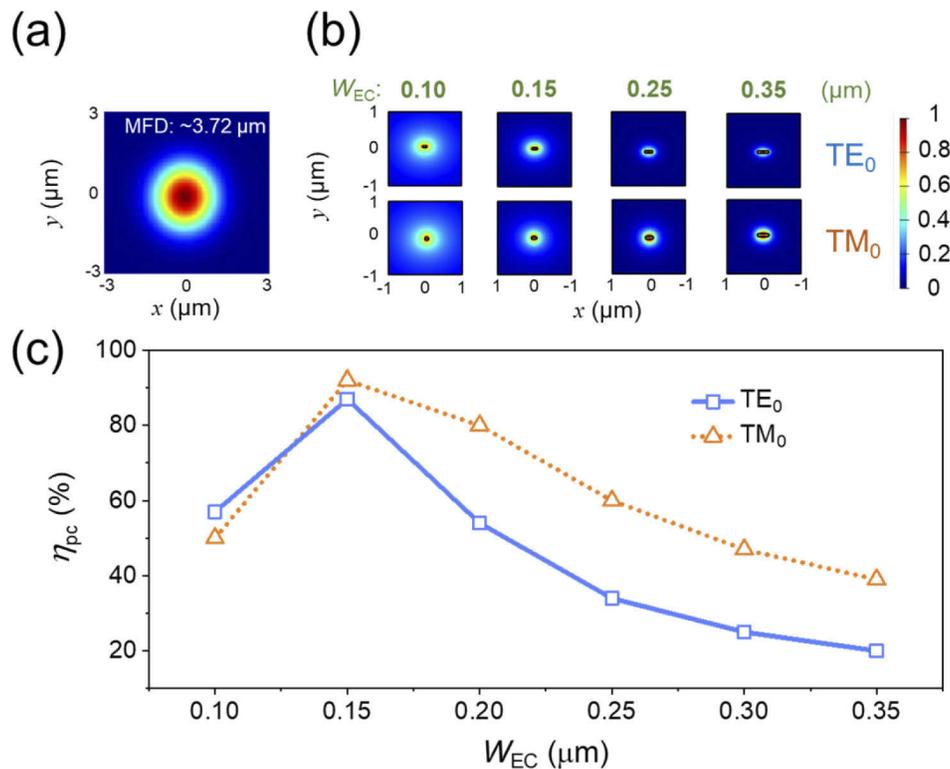

Fig. 2. Optimization of SiN2 tip width (W_{EC}) at $\lambda = 488$ nm. (a) Mode profile of Nufern S405-XP single-mode fiber at $\lambda = 488$ nm with a calculated mode field diameter (MFD) of 3.72 µm. (b) TE$_0$ and TM$_0$ mode profiles in SiN2 with respect to W_{EC}. (c) Calculated fiber-to-SiN2-tip power coupling efficiency (η_{pc}) as a function of W_{EC}.

2.2. Effect of SiN2 base width (W_{base}) and inverse taper length (L_{EC})

Next, we consider the mode conversion efficiency (η_{mc}) within the SiN2 inverse taper. W_{EC}, SiN2 base width (W_{base}) and the inverse taper length (L_{EC}) determine the η_{mc}. Meanwhile, W_{base} has a minimum width necessary to hybridize with the SiN1 waveguide mode for the adiabatic interlayer transition. Figure 3(a) shows the computed effective indices (n_{eff}) of the first four SiN2 eigenmodes (TE$_0$, TM$_0$, TE$_1$, TM$_1$), as a function of SiN2 waveguide width, and the n_{eff} of

the TE_0 and TM_0 modes of SiN1 waveguide width. Considering $W_{tip1} = 0.15$ µm, to hybridize the TE_0 and TM_0 modes in the two layers (i.e., for the effective indices to cross), we require $W_{base} \geq 0.54$ µm. Thus, we selected $W_{base} = 0.75$ µm.
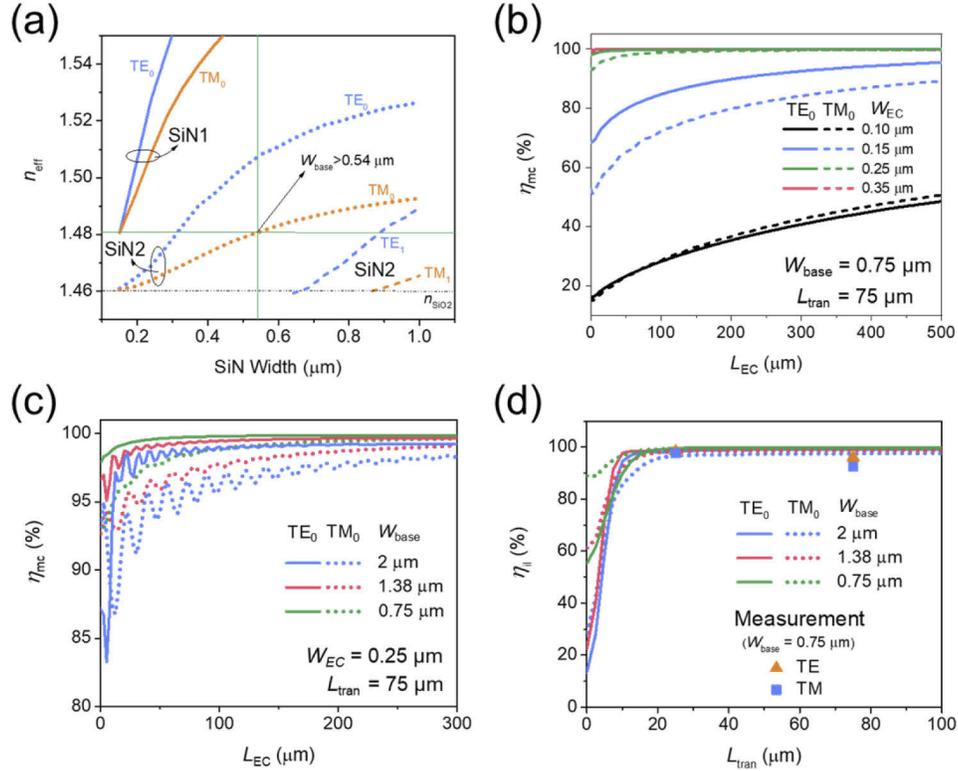

Fig. 3. Investigation and optimization of remaining design parameters. (a) Mode effective index (n_{eff}) of SiN1 and SiN2 as a function of SiN width. A $W_{base} \geq 0.54$ µm was determined to facilitate an adiabatic interlayer transition. (b) Calculated mode conversion efficiency (η_{mc}) of the bi-layer coupler as a function of W_{EC} and L_{EC} at a W_{base} and L_{tran} of 0.75 and 75 µm, respectively. (c) Calculated η_{mc} as a function of W_{base} and L_{EC} at a W_{EC} and L_{tran} of 0.25 and 75 µm. (d) Calculated SiN2-SiN1 transition efficiency (η_{il}) as a function of W_{base} and L_{tran}. Measurement results on cutback structures of SiN2-SiN1 transitions agree well with the calculated results.

We then investigated η_{mc} of the SiN2 inverse taper as a function of W_{EC}, W_{base} and L_{EC}. The calculation was performed using the Eigenmode Expansion (EME) method. In the calculation, the bi-layer coupler as in Fig. 1(a) was employed with $L_{tran} = 75$ µm, $W_{tip1} = W_{tip2} = 0.15$ µm and $W_{wg} = 0.38$ µm. The power transmission was evaluated from the squared magnitude of the S-parameters through the couplers [for all the calculations in Fig. 3(b-d)], which does not include η_{pc}. As an $L_{tran} = 75$ µm has been verified to have a > 99% power transmission [Fig. 3(d)], the obtained power transmission was considered equivalent to η_{mc} [for Fig. 3(b) and (c)]. The other dimensional parameters and material indices were identical to that used in the FDE calculation. Figure 3(b) shows the calculated η_{mc} as a function of W_{EC} and L_{EC}. The calculation reveals that η_{mc} increases with W_{EC} increasing from 0.10 to 0.25 µm at a fixed L_{EC}, due to a reduction in the difference between the W_{EC} and W_{base}. A longer L_{EC} leads to a higher power transmission as expected for adiabaticity. An $\eta_{mc} > 99\%$ can be achieved at an $L_{EC} > 100$ µm for $W_{EC} \geq 0.25$

μm. Hence, we choose $L_{EC} = 200$ μm as the focus of our designs and measurements in Section 3 (Fig. 4, 5 and 6) to keep a balance between η_{mc} and the device footprint.
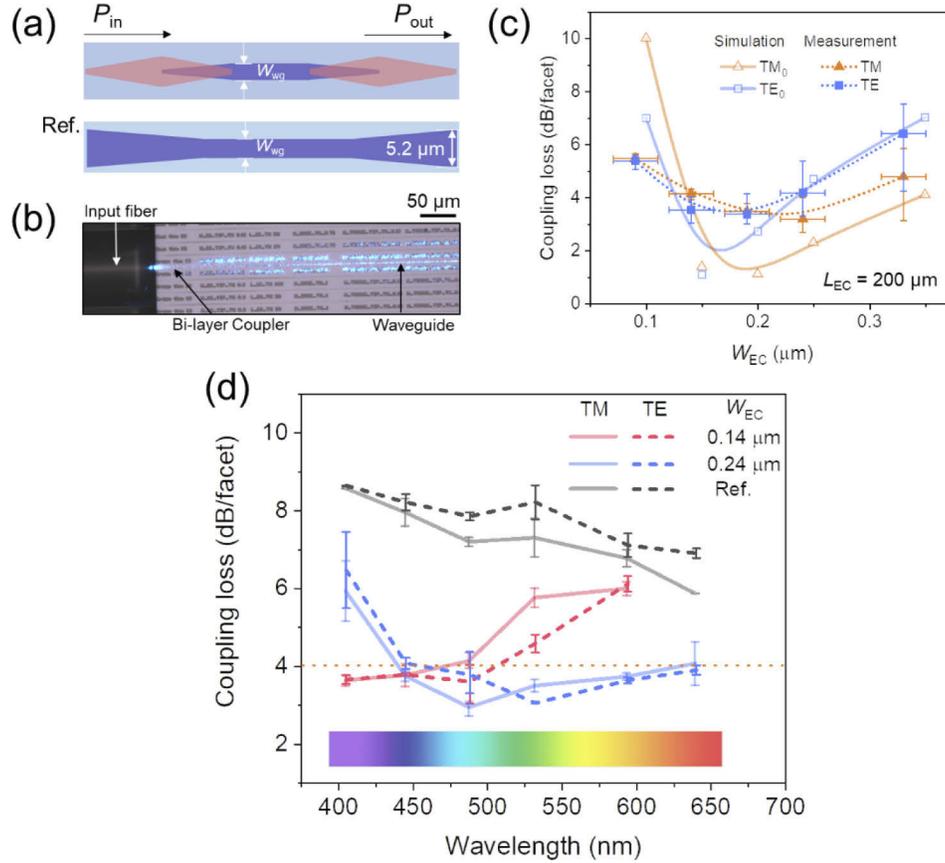

Fig. 4. Coupling loss measurement of bi-layer SiN edge couplers. (a) Schematic drawing of test structures with bi-layer couplers and reference single-layer tapered couplers. (b) An optical micrograph showing a bi-layer edge coupler under measurement at $\lambda = 488$ nm. (c) Measured coupling losses of bi-layer edge couplers as a function of W_{EC} at an L_{EC} of 200 μm at $\lambda = 488$ nm (dotted line). The results agree well with the simulated results considering both the fiber-to-tip coupling [η_{pc}, Fig. 2(c)] and the mode conversion efficiency in SiN2 inverse taper [η_{mc}, Fig. 3(b)]. (d) Measured coupling losses of the bi-layer edge couplers with W_{EC} of 0.14 and 0.24 μm (L_{EC}: 200 μm, W_{base}: 1 μm). The coupling losses from the reference single-layer couplers were also included as a benchmark.

Figure 3(c) shows the effect of W_{base} as a function of L_{EC} on the η_{mc} for $W_{base} \geq 0.54$ μm. Here, W_{EC} and L_{tran} were set to 0.25 μm and 75 μm, respectively. The maximum η_{mc} is reduced as W_{base} increases, but an η_{mc} over 95% was obtained for $W_{base} \leq 2$ μm at $L_{EC} \geq 100$ μm. The oscillations and reduced η_{mc} for $W_{base} = 2$ μm suggest power coupling into higher-order modes and power dissipation in the adiabatic transition to the fundamental modes in SiN1. We calculated n_{eff} for other wavelengths and verified that mode hybridization is possible for $\lambda \geq 405$ nm at a $W_{base} \geq 0.94$ μm (see Supplement 1, Fig. S5). We also verified that W_{base} has a negligible influence on the η_{mc} at this wavelength range within the W_{base} range of [0.94, 2.00] μm.
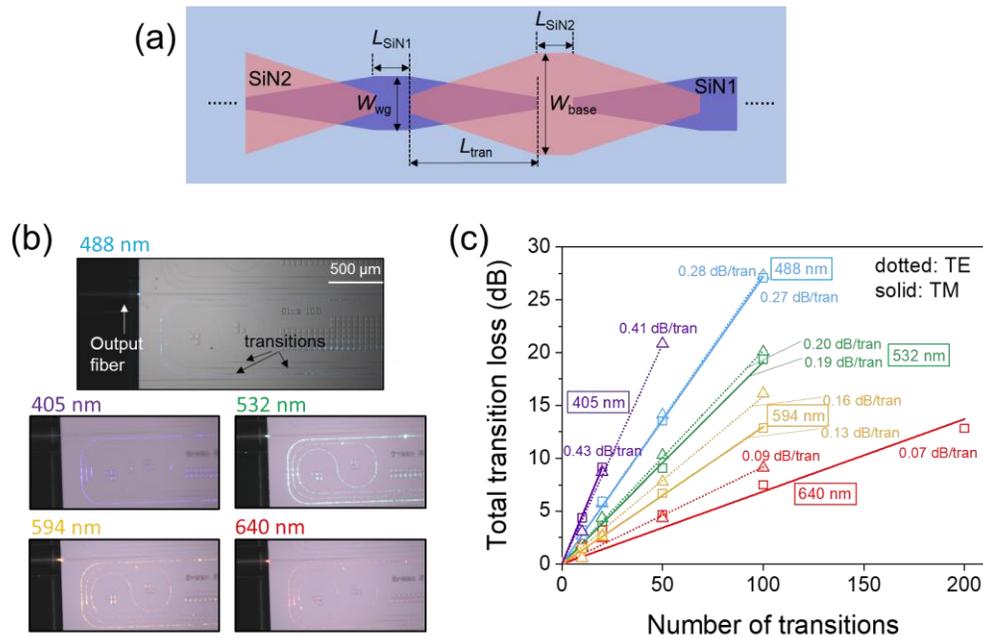
Fig. 5. Measurement of interlayer transition loss. (a) A schematic showing the SiN2-SiN1 interlayer transition cutback structure. (b) Optical micrographs of cutback structures incorporating interlayer transitions under measurement at different visible wavelengths. (c) Measured interlayer transition losses at different visible wavelengths.

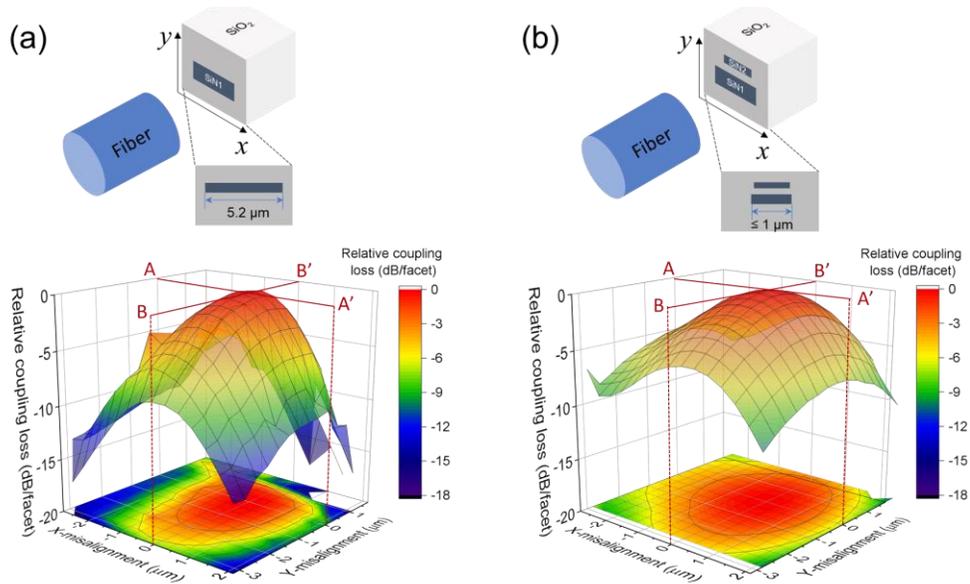**Fig. 6.** Relative coupling loss with respect to that at the optimal fiber-to-chip alignment, as a function of fiber misalignment for (a) a reference single-layer tapered edge coupler and (b) a bi-layer edge coupler (W_{EC}: 0.24 ± 0.02 µm, L_{EC}: 200 µm, W_{base}: 1 µm) at TM polarization. Contour plots as a projection of the 3-D plots are also shown at the bottom for an easy comparison.

2.3. Effect of SiN2-SiN1 transition length (L_{tran})

In this subsection, we optimized the SiN2-SiN1 transition length (L_{tran}). The same EME calculation was used. Here $W_{\text{EC}} = 0.25$ μm and $L_{\text{EC}} = 200$ μm to ensure an optimal power transmission at other parts of the coupler and thus the obtained total power transmission can be equivalent to the SiN2-SiN1 transition efficiency (η_{il}). An $\eta_{\text{il}} > 96\%$ was observed independent of W_{base} for $W_{\text{base}} \leq 2$ μm at a short $L_{\text{tran}} \geq 20$ μm [Fig. 3(d)]. Cutback test structures containing different numbers of SiN2-SiN1 transitions at L_{tran} of 25 and 75 μm were measured to extract the transmission efficiency of a single SiN2-SiN1 transition. A detailed illustration on the measurement setup and procedures can be found in Section 3. The measurement results agree well with the calculation results. Therefore, we selected bi-layer coupler test structures with $L_{\text{tran}} = 75$ μm for the subsequent measurements.

Finally, to calculate the final coupling efficiency of the couplers, we multiply η_{pc} [Fig. 2(c)] and η_{mc} [Fig. 3(b)] as a function of W_{EC} at an optimized $W_{\text{base}} = 0.75$ μm, $L_{\text{EC}} = 200$ μm and $L_{\text{tran}} = 75$ μm. The coupling efficiency is then converted to coupling power loss (dB/facet) and the results are shown as the hollow points with solid lines in Fig. 4(c). A minimum coupling loss of ~1 dB/facet is calculated for TE and TM at a W_{EC} of ~0.15 and ~0.20 μm, respectively. The decreasing coupling loss with decreasing W_{EC} at a wider W_{EC} is due to the improved fiber-to-tip coupling [see Fig. 2(c)], while the increasing loss with decreasing W_{EC} at a narrower W_{EC} can be explained by the reduced η_{mc} along the SiN2 inverse taper [see Fig. 3(b)]. The simulated coupling loss spectrum of the edge coupler with W_{EC} of ~0.24 μm is included in Supplement 1, Fig. S3. The design of bi-layer edge couplers comprising other materials and operating at other wavelengths can similarly follow the above principles, and a minimum coupling loss can occur at an inverse taper width where the trade-off between η_{pc} and η_{mc} is established.

3. Characterization of edge couplers

3.1. Measurement setup and methods

The couplers were characterized using a supercontinuum white light laser (NKT SuperK Extreme) and a continuous-wave multi-wavelength source (Coherent OBIS Galaxy). For the supercontinuum laser, a narrowband tunable optical filter (Photon etc. LLTF CONTRAST) was used to select specific wavelengths. We verified that the two light sources at a same wavelength resulted in similar measurement results, so the results can be directly compared irrespective of the light sources used (see Supplement 1, Fig. S1). Cleaved Nufern S405-XP single-mode fiber coupled the light into and out of the chip and guided the output to an optical power detector (Newport 818-SL-L) and meter (Newport 2936-R) for data collection. Both the fiber ends were mounted on 5-axis piezo-controlled micromanipulators for accurate alignment to the edge couplers. The alignment was computer controlled. In addition, a polarization controller (Thorlabs CPC900) was inserted into the input fiber path to control the polarization of the light into the couplers. To obtain the coupling loss, test structures with bi-layer couplers at both facets of the chip were measured [Fig. 4(a) top]. The coupling loss was obtained as $(P_{\text{out}}\text{-}P_{\text{prop}}\text{-}P_{\text{in}})/2$ (in dBm), where P_{in} and P_{out} denote the optical power into and out of the chip, and P_{prop} is the propagation loss in the 1.2-mm long SiN1 waveguide between the two couplers. SiN1 propagation losses measured at different wavelengths were summarized in Supplement 1, Fig. S2. At $\lambda = 488$ nm, P_{prop} is 4.0 ± 0.4 dB/cm for TM and 5.6 ± 0.5 dB/cm for TE for 0.38-μm wide waveguide. As a comparison, single layer (SiN1) tapered edge couplers were also designed and tested, where the taper was narrowed from 5.2 μm at the coupling facet to W_{wg} over a length of 400 μm [Fig. 4(a) bottom]. Figure 4(b) shows an optical micrograph of a bi-layer coupler test structure under measurement at $\lambda = 488$ nm.

The cutback method was utilized to characterize the SiN1 propagation loss and SiN2-SiN1 transition loss. Figure 5(a) shows a schematic of the SiN2-SiN1 interlayer transition cutback

structure, where $W_{base} = 0.75$ µm. $W_{wg} = 0.38$ µm was used in the cutback structures for measurements at $\lambda = 405$, 445, 488 and 532 nm, while $W_{wg} = 0.52$ µm was used for $\lambda = 594$ and 640 nm. $L_{SiN2} = 5$ µm denotes the length of SiN2 waveguide between the SiN1-SiN2 and SiN2-SiN1 transitions. Measurements of the cutback structures containing the SiN2 waveguides found the SiN2 propagation loss to be negligible compared to the transition loss. L_{SiN1} was randomized to avoid resonant reflections between transitions. Figure 5(b) shows optical micrographs of a transition cutback structure with input at several wavelengths. In the following, the measured coupling losses were collected from 3 chips far apart (>10 cm) across the wafer, with one respective device on each chip. W_{EC} values were determined from TEM cross-sectional images.

3.2. Results and discussion

To verify the calculated coupling loss of the bi-layer SiN couplers (solid lines in Fig. 4(c)), the test structures as in Fig. 4(a) top ($W_{wg} = 0.38$ µm) were measured as a function of W_{EC}, where W_{base} (0.75 µm), L_{EC} (200 µm) and L_{tran} (75 µm) are identical to that in the calculation. The results are shown as the solid points with dotted lines in Fig. 4(c). The measurement results agree reasonably well with the calculation results, which validated our design and optimization approach discussed in Section 2. The lowest coupling loss for TM polarization (3.2 ± 0.5 dB/facet) was obtained at a W_{EC} of 0.24 ± 0.02 µm, and a polarization-insensitive coupling was achieved at a W_{EC} of 0.19 ± 0.02 µm, where the coupling losses are 3.5 ± 0.3 and 3.4 ± 0.8 dB/facet for TM and TE, respectively. The higher minimum coupling loss compared to simulation can be attributed to the fabrication-induced imperfections in the coupler structure.

The bi-layer coupler testing structures ($L_{EC} = 200$ µm, $L_{tran} = 75$ µm and $W_{base} = 1$ µm, $W_{wg} = 0.38$ µm) were also measured at several wavelengths (405, 445, 488, 532, 594 and 640 nm) to characterize the optical bandwidth performance, as shown in Fig. 4(d). A coupler with W_{EC} of 0.24 ± 0.02 µm exhibited a coupling loss ≤ 4 dB/facet from $\lambda = 445$ to 640 nm, which covers most of the visible spectrum from blue to red colors. Simulated coupling loss (determined from $\eta_{pc} \times \eta_{mc}$, see Section 2) revealed a similar trend with the measurement results [see Supplement 1, Fig. S3 (a)]. The higher loss at shorter wavelengths was due to the compromised fiber-to-tip coupling efficiency [see Supplement 1, Fig. S3 (b)]. Hence, a lower coupling loss at the deep blue and violet wavelengths can be achieved by adopting a narrower W_{EC}. A coupler with a W_{EC} of 0.14 ± 0.02 µm had a coupling loss < 4 dB/facet at $\lambda = 405$ and 445 nm. Therefore, the bi-layer coupler design concept can achieve a low-loss coupling ≤ 4.0 dB/facet at any wavelength in the visible spectrum. In contrast, the single-layer SiN1 tapered edge couplers exhibited a ~3–5 dB higher coupling loss per facet across the visible spectrum. Meanwhile, compared to the performance of state-of-the-art visible-light grating couplers, the bi-layer design also exhibited a superior coupling efficiency spanning across a wider optical bandwidth. For example, Song *et al.* [42] reported coupling losses of 9.1 and 6.8 dB at 532 and 644 nm, respectively, for SiN grating couplers. Although Arefin *et al.* [43] declared a similar coupling loss at 450 nm, the corresponding 3-dB optical bandwidth was limited to ~30 nm. All these comparisons highlight the superior overall performance of the bi-layer SiN edge couplers in terms of coupling efficiency and bandwidth. A detailed summary of the measured coupling loss as a function of W_{EC} and L_{EC} at different wavelengths can be found in Supplement 1, Fig. S4.

Figure 5(c) shows the measured SiN2-SiN1 transition loss at 5 selected wavelengths (405, 488, 532, 594 and 640 nm) across the visible spectrum. The transition loss was < 0.5 dB per interlayer transition for the measured wavelengths. Furthermore, the transition loss increased with a decreasing wavelength. This is due to the increase of the lower bound of W_{base} with a decreasing wavelength (see Supplement 1, Fig. S5) for mode hybridization with SiN1. At $\lambda = 405$ nm, the lower bound of W_{base} exceeds 0.75 µm, indicating an unmatched phase between SiN1 and SiN2 during the transition. Therefore, the transition loss at shorter wavelengths can be further reduced by widening the W_{base}.

We further characterized the fiber alignment tolerance of the bi-layer couplers. Figure 6 shows a comparison of the alignment tolerance at TM polarization at $\lambda = 488$ nm between a bi-layer ($W_{EC} = 0.24 \pm 0.02$ μm) and a single layer coupler. The contour maps were obtained via scanning the coupling loss as a function of both the horizontal [x-direction, Fig. 6(a, b) top] and vertical [y-direction, Fig. 6(a, b) top] displacements of the micromanipulator mounted with the input fiber. The relative coupling losses and the corresponding fiber misalignment displacements were then determined with respect to the coupling loss and the micromanipulator position at the optimal fiber-to-coupler alignment (i.e., the position with lowest coupling loss), respectively. The bi-layer coupler provides a 1-dB alignment tolerance of ±0.88 μm horizontally (AA', along x-direction) and ±1.15 μm vertically (BB', along y-direction). This is ±0.30 μm wider than that of the single layer coupler horizontally and ±0.22 μm wider vertically. In addition, the alignment tolerance is comparable for TE polarization, where the 1-dB tolerance is ±0.20 μm wider horizontally but ±0.35 μm narrower vertically for the bi-layer coupler (see Supplement 1, Fig. S6). The corresponding 3-dB tolerance is ±1.60 and ±1.26 μm horizontally, and ±2.05 and ±1.45 μm vertically, for the bi-layer and single layer coupler, respectively, at TM; while at TE, the 3-dB tolerance is correspondingly ±1.59 and ±1.16 μm horizontally, and ±1.50 and ±2.05 μm vertically.

4. Conclusion

In conclusion, we have demonstrated low-loss and broadband bi-layer SiN edge couplers operating in the visible light spectrum. The bi-layer approach alleviates the trade-off between the fiber coupling efficiency and on-chip integration density. Key dimensional parameters determining the coupling efficiency of the bi-layer coupler have been discussed and optimized. A lower bound on W_{base} is required to facilitate a low-loss interlayer transition. Simulation finds that the coupling efficiency depends on the trade-off between η_{pc} and η_{mc}. Measured coupling loss at $\lambda = 488$ nm as a function of W_{EC} agreed well with simulations. A low coupling loss ≤ 4 dB/facet has been observed across the visible spectrum, in which the SiN2-SiN1 interlayer transition accounted for < 0.5 dB of the loss. The coupling loss was ~3–5 dB lower compared to single layer SiN1 tapered edge couplers. In addition, the bi-layer coupler exhibits a superior alignment tolerance compared to the single layer coupler at TM polarization. The results show that the bi-layer SiN edge couplers are promising for many PIC applications across the visible spectrum. The design can be extended to other combinations of materials in the bi-layer structure, and potentially to multi-layer structures, for coupling with visible-light fibers of different MFDs.

Disclosures. The authors declare no conflicts of interest.

Data availability. Data underlying the results presented in this paper are not publicly available at this time but may be obtained from the authors upon reasonable request.

Supplemental document. See Supplement 1 for supporting content.

References

1. L. C. Moreaux, D. Yatsenko, W. D. Sacher, J. Choi, C. Lee, N. J. Kubat, R. J. Cotton, E. S. Boyden, M. Z. Lin, L. Tian, A. S. Tolias, J. K. S. Poon, K. L. Shepard, and M. L. Roukes, "Integrated Neurophotonics: Toward Dense Volumetric Interrogation of Brain Circuit Activity—at Depth and in Real Time," Neuron **108**(1), 66–92 (2020).
2. W. Sacher, F.-D. Chen, H. Moradi-Chameh, X. Luo, A. Fomenko, P. Shah, T. Lordello, X. Liu, I. Felts Almog, J. Straguzzi, T. Fowler, Y. Jung, T. Hu, J. Jeong, A. Lozano, P. Lo, T. Valiante, L. Moreaux, J. Poon, and M. Roukes, "Implantable photonic neural probes for light-sheet fluorescence brain imaging," Neurophotonics **8**(02), 025003 (2021).
3. E. Shim, Y. Chen, S. Masmanidis, and M. Li, "Multisite silicon neural probes with integrated silicon nitride waveguides and gratings for optogenetic applications," Sci. Rep. **6**(1), 22693 (2016).
4. A. Mohanty, Q. Li, M. A. Tadayon, S. P. Roberts, G. R. Bhatt, E. Shim, X. Ji, J. Cardenas, S. A. Miller, A. Kepecs, and M. Lipson, "Reconfigurable nanophotonic silicon probes for sub-millisecond deep-brain optical stimulation," Nat. Biomed. Eng. **4**(2), 223–231 (2020).

5. V. Lanzio, G. Telian, A. Koshelev, P. Micheletti, G. Presti, E. D'Arpa, P. De Martino, M. Lorenzon, P. Denes, M. West, S. Sassolini, S. Dhuey, H. Adesnik, and S. Cabrini, "Small footprint optoelectrodes using ring resonators for passive light localization," Microsyst. Nanoeng. **7**(1), 40 (2021).
6. R. J. Niffenegger, J. Stuart, C. Sorace-Agaskar, D. Kharas, S. Bramhavar, C. D. Bruzewicz, W. Loh, R. T. Maxson, R. McConnell, D. Reens, G. N. West, J. M. Sage, and J. Chiaverini, "Integrated multi-wavelength control of an ion qubit," Nature **586**(7830), 538–542 (2020).
7. K. K. Mehta, C. Zhang, M. Malinowski, T. L. Nguyen, M. Stadler, and J. P. Home, "Integrated optical multi-ion quantum logic," Nature **586**(7830), 533–537 (2020).
8. M. Raval, A. Yaacobi, and M. R. Watts, "Integrated visible light phased array system for autostereoscopic image projection," Opt. Lett. **43**(15), 3678–3681 (2018).
9. J. Notaros, M. Raval, M. Notaros, and M. R. Watts, "Integrated-Phased-Array-Based Visible-Light Near-Eye Holographic Projector," in *Conference on Lasers and Electro-Optics*, OSA Technical Digest (Optical Society of America, 2019), STu3O.4.
10. M. Chul Shin, A. Mohanty, K. Watson, G. R. Bhatt, C. T. Phare, S. A. Miller, M. Zadka, B. S. Lee, X. Ji, I. Datta, and M. Lipson, "Chip-scale blue light phased array," Opt. Lett. **45**(7), 1934–1937 (2020).
11. M. Papes, P. Cheben, D. Benedikovic, J. H. Schmid, J. Pond, R. Halir, A. Ortega-Monux, G. Wanguemert-Perez, W. N. Ye, D. X. Xu, S. Janz, M. Dado, and V. Vasinek, "Fiber-chip edge coupler with large mode size for silicon photonic wire waveguides," Opt. Express **24**(5), 5026–5038 (2016).
12. V. R. Almeida, R. R. Panepucci, and M. Lipson, "Nanotaper for compact mode conversion," Opt. Lett. **28**(15), 1302–1304 (2003).
13. S. H. Tao, J. Song, Q. Fang, M. B. Yu, G. Q. Lo, and D. L. Kwong, "Improving coupling efficiency of fiber-waveguide coupling with a double-tip coupler," Opt. Express **16**(25), 20803–20808 (2008).
14. Y. Wang, W. Shi, X. Wang, Z. Lu, M. Caverley, R. Bojko, L. Chrostowski, and N. A. F. Jaeger, "Design of broadband subwavelength grating couplers with low back reflection," Opt. Lett. **40**(20), 4647–4650 (2015).
15. Z. Xiao, F. Luan, T.-Y. Liow, J. Zhang, and P. Shum, "Design for broadband high-efficiency grating couplers," Opt. Lett. **37**(4), 530–532 (2012).
16. W. D. Sacher, Y. Huang, L. Ding, B. J. Taylor, H. Jayatilleka, G. Q. Lo, and J. K. Poon, "Wide bandwidth and high coupling efficiency Si3N4-on-SOI dual-level grating coupler," Opt. Express **22**(9), 10938–10947 (2014).
17. X. Mu, S. Wu, L. Cheng, and H. Y. Fu, "Edge Couplers in Silicon Photonic Integrated Circuits: A Review," Appl. Sci. **10**(4), 1538 (2020).
18. R. Marchetti, C. Lacava, L. Carroll, K. Gradkowski, and P. Minzioni, "Coupling strategies for silicon photonics integrated chips [Invited]," Photonics Res. **7**(2), 201 (2019).
19. W. D. Sacher, X. Luo, Y. Yang, F. D. Chen, T. Lordello, J. C. C. Mak, X. Liu, T. Hu, T. Xue, P. Guo-Qiang Lo, M. L. Roukes, and J. K. S. Poon, "Visible-light silicon nitride waveguide devices and implantable neurophotonic probes on thinned 200 mm silicon wafers," Opt. Express **27**(26), 37400–37418 (2019).
20. J. Cardenas, C. B. Poitras, K. Luke, L.-W. Luo, P. A. Morton, and M. Lipson, "High Coupling Efficiency Etched Facet Tapers in Silicon Waveguides," IEEE Photonics Technol. Lett. **26**(23), 2380–2382 (2014).
21. N. Lin, S. Hassan, X. Zhao, A. Veeraraghavan, and J. Robinson, "High coupling efficiency, passive alignment setup for visible-range fiber-to-waveguide edge coupling," J. Nanophotonics **14**(4), 046018 (2020).
22. A. T. Mashayekh, T. Klos, D. Geuzebroek, E. Klein, T. Veenstra, M. Buscher, F. Merget, P. Leisching, and J. Witzens, "Silicon nitride PIC-based multi-color laser engines for life science applications," Opt. Express **29**(6), 8635–8653 (2021).
23. A. Mashayekh, T. Klos, S. Koch, F. Merget, D. Geuzebroek, E. Klein, T. Veenstra, M. Büscher, P. Leisching, and J. Witzens, *Miniaturized PIC multi-color laser engines for the life sciences*, SPIE OPTO (SPIE, 2019), Vol. 10922.
24. N. Chauhan, A. Isichenko, K. Liu, J. Wang, Q. Zhao, R. O. Behunin, P. T. Rakich, A. M. Jayich, C. Fertig, C. W. Hoyt, and D. J. Blumenthal, "Visible light photonic integrated Brillouin laser," Nat. Commun. **12**(1), 4685 (2021).
25. B. Ben Bakir, A. V. de Gyves, R. Orobtchouk, P. Lyan, C. Porzier, A. Roman, and J. M. Fedeli, "Low-Loss (<1 dB) and Polarization-Insensitive Edge Fiber Couplers Fabricated on 200-mm Silicon-on-Insulator Wafers," IEEE Photonics Technol. Lett. **22**(11), 739–741 (2010).
26. M.-J. Picard, C. Latrasse, C. Larouche, Y. Painchaud, M. Poulin, F. Pelletier, and M. Guy, *CMOS-compatible spot-size converter for optical fiber to sub-um silicon waveguide coupling with low-loss low-wavelength dependence and high tolerance to misalignment*, SPIE OPTO (SPIE, 2016), Vol. 9752.
27. M. W. Puckett and N. A. Krueger, "Broadband, ultrahigh efficiency fiber-to-chip coupling via multilayer nanophotonics," Appl. Opt. **60**(15), 4340–4344 (2021).
28. H. Park, S. Kim, J. Park, J. Joo, and G. Kim, "A fiber-to-chip coupler based on Si/SiON cascaded tapers for Si photonic chips," Opt. Express **21**(24), 29313–29319 (2013).
29. Y. Maegami, R. Takei, E. Omoda, T. Amano, M. Okano, M. Mori, T. Kamei, and Y. Sakakibara, "Spot-size converter with a SiO(2) spacer layer between tapered Si and SiON waveguides for fiber-to-chip coupling," Opt. Express **23**(16), 21287–21295 (2015).
30. M. Pu, L. Liu, H. Ou, K. Yvind, and J. M. Hvam, "Ultra-low-loss inverted taper coupler for silicon-on-insulator ridge waveguide," Opt. Commun. **283**(19), 3678–3682 (2010).
31. K. Kruse and C. T. Middlebrook, "Polymer taper bridge for silicon waveguide to single mode waveguide coupling," Opt. Commun. **362**, 87–95 (2016).

32. K. Ku and M. M. Lee, "Wide-Band Optical Mode Converters for Coupling Between Fibers and Silicon Photonic Wires With Large Misalignment Tolerance," J. Lightwave Technol. **31**(10), 1616–1620 (2013).

33. T. Barwicz and Y. Taira, "Low-Cost Interfacing of Fibers to Nanophotonic Waveguides: Design for Fabrication and Assembly Tolerances," IEEE Photonics J. **6**(4), 1–18 (2014).

34. A. Khilo, M. A. Popović, M. Araghchini, and F. X. Kärtner, "Efficient planar fiber-to-chip coupler based on two-stage adiabatic evolution," Opt. Express **18**(15), 15790–15806 (2010).

35. B. Desiatov, A. Shams-Ansari, M. Zhang, C. Wang, and M. Lončar, "Ultra-low-loss integrated visible photonics using thin-film lithium niobate," Optica **6**(3), 380–384 (2019).

36. T. J. Lu, M. Fanto, H. Choi, P. Thomas, J. Steidle, S. Mouradian, W. Kong, D. Zhu, H. Moon, K. Berggren, J. Kim, M. Soltani, S. Preble, and D. Englund, "Aluminum nitride integrated photonics platform for the ultraviolet to visible spectrum," Opt. Express **26**(9), 11147–11160 (2018).

37. J. T. Choy, J. D. B. Bradley, P. B. Deotare, I. B. Burgess, C. C. Evans, E. Mazur, and M. Lončar, "Integrated TiO2 resonators for visible photonics," Opt. Lett. **37**(4), 539–541 (2012).

38. C. Xiong, W. H. Pernice, and H. X. Tang, "Low-loss, silicon integrated, aluminum nitride photonic circuits and their use for electro-optic signal processing," Nano Lett. **12**(7), 3562–3568 (2012).

39. C. Sorace-Agaskar, D. Kharas, S. Yegnanarayanan, R. T. Maxson, G. N. West, W. Loh, S. Bramhavar, R. J. Ram, J. Chiaverini, J. Sage, and P. Juodawlkis, "Versatile Silicon Nitride and Alumina Integrated Photonic Platforms for the Ultraviolet to Short-Wave Infrared," IEEE J. Sel. Top. Quantum Electron. **25**(5), 1–15 (2019).

40. G. N. West, W. Loh, D. Kharas, C. Sorace-Agaskar, K. K. Mehta, J. Sage, J. Chiaverini, and R. J. Ram, "Low-loss integrated photonics for the blue and ultraviolet regime," APL Photonics **4**(2), 026101 (2019).

41. M. Belt, M. L. Davenport, J. E. Bowers, and D. J. Blumenthal, "Ultra-low-loss Ta_2O_5-core/SiO_2-clad planar waveguides on Si substrates," Optica **4**(5), 532–536 (2017).

42. J. H. Song, T. D. Kongnyuy, B. Troia, S. S. Saseendran, P. Soussan, R. Jansen, and X. Rottenberg, "Grating devices on a silicon nitride technology platform for visible light applications," OSA Continuum **2**(4), 1155–1165 (2019).

43. R. Arefin, S. Ramachandra, H. Jung, S. M. N. Hasan, W. You, S. Dwivedi, and S. Arafin, "Gallium- and Silicon Nitride-Based Photonic Integrated Circuits for Visible Wavelengths," in *Conference on Lasers and Electro-Optics*, OSA Technical Digest (Optical Society of America, 2020), JTh2B.19.